

---

# MHD FLOW REGIMES IN ANNULAR CHANNEL

---

**Kaiyu Zhang**  
School of Astronautics  
Beihang University  
Beijing, 102206, China  
zkyae@buaa.edu.cn

**Yibai Wang**  
School of Astronautics  
Beihang University  
Beijing, 102206, China

**Haibin Tang**  
School of Space and Environment  
Beihang University  
Beijing, 102206, China  
thb@buaa.edu.cn

**Lijun Yang**  
School of Astronautics  
Beihang University  
Beijing, 102206, China

September 23, 2021

## ABSTRACT

One method and two results are contributed to the complete understanding about MHD laminar flow in annular channel with transverse magnetic field in this paper. In terms of the method, a computationally cheap semi-analytic algorithm is developed based on spectral method and perturbation expansion. By virtue of the fast computation, dense cases with almost continuous varying Hartmann number  $M$ , Reynolds number  $Re$  and cross-section ratio  $\eta$  are calculated to explore the flow patterns that are missed in previous research. In terms of the results of inertialess regime, we establish the average velocity map and electric-flow coupling delimitation in  $\eta$ - $M$  space. Seven phenomenological flow patterns and their analytical approaches are identified. In terms of the results of inertial regime, we examine the law of decreasing order-of-magnitude of inertial perturbation on primary flow with increasing Hartmann number. The proposed semi-analytic solution coincides with the  $Re^2/M^4$  suppression theory of Baylis & Hunt (*J. Fluid Mech.*, vol. 43, 1971, pp. 423-428) in the case of  $M < 40$ . When  $M > 40$ , the pair of trapezoid vortices of secondary flow begins to crack and there is therefore a faster drop in inertial perturbation as  $Re^2/M^5$ , which is a new suppression theory. When  $M > 80$ , the anomalous reverse vortices are fully developed near Shercliff layers resulting in the weaker suppression mode of  $Re^2/M^{2.5}$ , which confirms the theoretical prediction of Tabeling & Chabrier (*J. Fluid Mech.*, vol. 103, 1981, pp. 225-239).

## 1 Introduction

Magnetohydrodynamic (MHD) flow in the annular channel with transverse magnetic field is of great interest due to the experimental search for magneto-rotational-instability (MRI) in astrophysics Balbus and Hawley (1998), MHD dynamo in geophysics Larmor (1919), and swirling actuators in engineering Zhang et al. (2020). The idea of this apparatus, of which schematic is shown in figure 1, is using radial electric field and axial magnetic field to make azimuthal Lorentz forces and drive the azimuthal rotation of conductive fluids (primary flow). At the same time, centrifugal force causes radial velocity transport, and then the secondary eddies emerge on the radial-axial plane (secondary flow).

The relevant research can be traced back to the experiment of Baylis (1964), in which the onset of instability was detected through the drop in measured voltage. However, at that time, it was unclear whether this onset point was caused by the enhancement of secondary flow or transition into turbulence. Later, Baylis and Hunt (1971) established the first analytical solution to the velocity profile of the primary rotation flow at great Hartman number  $M$  using boundary-layer-analysis method. This research theoretically proved that increasing  $M$  can suppress the magnitude of inertial force and secondary flow to an extent of  $Re^2/M^4$ , and thus stabilize the primary flow. This  $Re^2/M^4$  law has been commonly used to judge whether the secondary flow is coupled into the laminar-to-turbulence transition in later research. Tabeling and Chabrier (1981) performed perturbation expansion of curvature of the annular channel and recalculated the secondary flow. His analytical study identified there will be the reverse vortexes adjacent to the conductive walls in secondary flow if the Hartmann number is great. And the presence of reverse vortexes leads to a weaker suppression mode of inertial effect, which is  $Re^2/M^{2.5}$ . Shortly afterwards, Tabeling (1982) experimentally investigated the sequences of Taylor instability caused by centrifugal force and secondary flow before the onset of turbulence in the case of  $M \sim 10^2$ . On the other hand, Moresco and Alboussière (2004) conducted the experiment with by far higher Hartmann number ( $M 10^3$ )

for the purpose of the secondary-flow-free turbulence transition. This experiment indicated the critical parameter for the turbulent onset is  $Re/M \approx 380$ . Besides, the laminar part of experiment data showed the friction factor  $F \approx 2M/Re$  for the case of square cross-section, which has been an important result used to verify the numerical or analytical laminar models.

Khalzov et al. (2006) threw light on the global instability modes without dissipation effect by the method of spectral analysis, and found that the flow can be stable to the axisymmetric mode for certain geometric parameters of the device. Years later, Khalzov et al. (2010), Vantighem and Knaepen (2011) and Zhao and Zikanov (2012) performed detailed numerical investigation. Their numerical simulations observed the coexistence of Hartmann layers and Shercliff layers in primary flow and the morphology of toroidal vortices in secondary flow. These three simulations came to a consistent conclusion that toroidal vortices of secondary flow can strengthen azimuthal velocity of primary flow on radially outer side, but weaken that on inner side. Particularly, for the case with  $M = 100$  and  $M = 400$ , Vantighem and Knaepen (2011) confirmed the presence of reverse vortexes adjacent to the conductive walls as predicted by Tabeling and Chabrierie (1981). The Doppler velocimetry started to be used in the relevant research since the experiment of Stelzer et al. (2015), in which the structure of electrodes was modified in the hope of observing Sheriff-layer-free flow. With the Doppler velocimetry and the common electrodes, Boisson et al. (2017) experimentally confirmed the toroidal vortices that had been calculated by previous numerical simulations for the first time. Furthermore, he identified that duct geometry has dramatic effect on the frequency of instability waves, which shed new light on the geometry effect, while all previous numerical research take the fixed cross-section of which high-width ratio  $\eta$  is 1. Recently, to extend our knowledge into large  $\eta$  case, Poyé et al. (2020) employed numerical simulation for much more cases with the varied cross-section shapes, and then identified fruitful scale laws for different flow structures. Specifically, he pinpointed that it is possible that Hartmann layers exist while Shercliff layers overlap when  $\eta \gg 1$ , while the opposite case of  $\eta \ll 1$  was recommended as future study.

Against this background, it is true that a large number of experimental and numerical data have been available for this type of MHD channel flow. But even the laminar case is far from thoroughly understood. There are at least three problems to be tackled before completing the research about the MHD annular laminar flow.

- 1 **In inertialess regime, how many flow patterns there are?** the research of Poyé et al. (2020) indicates that different geometric parameters and Hartmann numbers lead to the flow patterns, of which boundary layers are different from the analytical theory of Baylis and Hunt (1971). However, the operating conditions of previous simulations and experiments are limited. Most of the combination of geometric parameters and Hartmann numbers have never been reached. Moreover, it is still not certain that how many flow patterns there are and what features they have.
- 2 **In inertial regime, how the vortexes develop in secondary flow by degrees?** the simulation of Khalzov et al. (2010) show there is only one pair of vortexes in secondary flow with moderate Hartmann number  $M = 30$ . The simulation of Zhao and Zikanov (2012) show there are two pairs of vortexes when  $M \approx 100$ . The simulation of Vantighem and Knaepen (2011) show there will be thin reverse vortexes apart from the two pair of main vortexes when  $M \approx 400$ . However, because the values of Hartmann number in these simulations are scattered, it is still not clear how the vortexes develop in secondary flow as Hartmann number increases. And we do not know the exact  $M$  criticality when vortexes break and reverse vortexes emerge neither.
- 3 **In terms of the criteria of inertial and inertialess regime, which scale law shall be applied?** The estimate formula is important to the MRI research, because researchers prefer no effect of secondary flow on the profile of primary flow. The consensus among previous research is that increasing Hartmann number can suppress inertial effect. The analytical analysis of Baylis and Hunt (1971) believe the order of  $M$  in the suppression is  $-4$ , while Tabeling and Chabrierie (1981) thought  $M^{-4}$  theory underestimate the axial velocity near Shercliff layers and should be modified into  $M^{-2.5}$ . However, most of later research applies  $M^{-4}$  theory to the estimation of inertial effect, while  $M^{-2.5}$  theory has not been given enough attention. The point is, to our best knowledge, there is neither numerical nor experimental data conforming either of the two theories. It seems that each of the two theories is supposed to have a specific sphere of application, which is still unknown to the scientific community.

It is clear that the solution to the three problems entails studying numerous physical cases with almost continuously changing physical and geometric parameters, which can hardly be achieved by existing research methods of numerical simulations. In this paper, a novel semi-analytic method is proposed to meet the demands. The description of this algorithm is recorded in section 3. In section 4, we will try to use this new method to cover all existing experimental and numerical data for inertialess regime, and meanwhile conduct a comprehensive exploration of the flow patterns to answer the first question. Section 5 is devoted to the inertial regime. We will harmonize the two disputed laws of inertial effect to answer the last two questions.

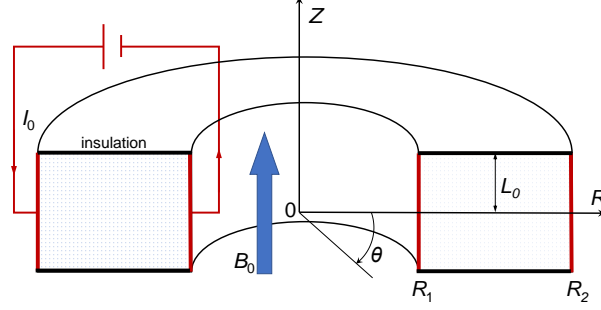


Figure 1: Scheme of the MHD annular duct. The current investigation is on the  $(r, z)$  plane.

## 2 Equations of Problem

We consider the incompressible dissipative MHD fluid in the annular channel with a rectangular cross-section as shown in Fig.1. We set the cylindrical coordinate system  $R, \theta, Z$  whose origin is at the symcenter of the toroid. The outer radius and inner radius are  $R_2$  and  $R_1$ , respectively. The height of toroid is bisected by the  $R$ - $\theta$  plane into two halves with the length of  $L_0$ . The symbol notations are presented in table 1. The walls at  $R = R_1$  and  $R = R_2$  are called side walls, which are conductive; the walls at  $Z = \pm 1$  are called end walls, which are insulative. In this system, the external magnetic field  $B_0$  is imposed axially. And the current goes through the duct from outer to inner, inducing the azimuthal self magnetic fields.

This study assumes that:

- the flow is laminar and steady.
- the steady field variables are axisymmetric, namely  $\partial/\partial\theta \equiv 0$  for any physical quantity.
- the induced magnetic field can be ignored compared with  $B_0$  (Davidson, 2016). Mathematically, magnetic Reynolds number  $Re_m \ll 1$  and magnetic Prandtl number  $Pr_m \ll 1$ .

With the above assumptions, the dimensional incompressible dissipative MHD equations are written as follows:

$$\nabla \cdot \mathbf{V} = 0, \quad (1a)$$

$$\nabla \cdot \mathbf{J} = 0, \quad (1b)$$

$$\rho(\mathbf{V} \cdot \nabla)\mathbf{V} = -\nabla p + \mathbf{J} \times \mathbf{B}_0 + \mu \nabla^2 \mathbf{V}, \quad (1c)$$

$$\nabla \times \mathbf{J}/\sigma = \nabla \times (\mathbf{V} \times \mathbf{B}_0). \quad (1d)$$

Nondimensionalize length, velocity, current density by the scale of  $L_0$ ,  $V_0 \equiv I_0/(4\pi L_0 \sqrt{\sigma \mu})$ ,  $J_0 \equiv I_0/(4\pi L_0^2)$ , respectively, as follows:

$$r = R/L_0, \quad z = Z/L_0, \quad \mathbf{v} = \mathbf{V}/V_0, \quad \mathbf{j} = \mathbf{J}/J_0. \quad (2)$$

In terms of  $\mathbf{v}$ , we define  $u$  as the angular momentum and  $w$  as stream functions of the velocity. Thanks to the axisymmetric assumption, we get:

$$v_r = -\frac{\partial w}{r \partial z}, \quad v_\theta = \frac{u}{r}, \quad v_z = \frac{\partial w}{r \partial r}. \quad (3)$$

In terms of  $\mathbf{j}$ , we define  $h$  as stream functions of the current density. Based on the induction-less assumption combined with equation 1 b, we get:

$$j_r = -\frac{\partial h}{r \partial z}, \quad j_\theta = M \frac{\partial w}{r \partial z}, \quad j_z = \frac{\partial h}{r \partial r}. \quad (4)$$

In this context, the original MHD equations are transformed into:

$$0 = \Delta^* u + M \frac{\partial h}{\partial z} + Re \frac{u \otimes w}{r}, \quad (5a)$$

$$0 = \Delta^* h + M \frac{\partial u}{\partial z}, \quad (5b)$$

$$0 = \Delta^* \Delta^* w - M^2 \frac{\partial^2 w}{\partial z^2} - r Re \left( w \otimes \frac{\Delta^* w}{r^2} + \frac{1}{r^3} \frac{\partial u^2}{\partial z} \right), \quad (5c)$$

| Notions                                      | Dimensional                                 | Non-dimensional   |
|--|---|---|
|  | constants                                   |   |
| half of the duct height (scaling the length) | $L_0$                                       |   |
| inner radius                                 | $R_1$                                       | $r_1 \equiv R_1/L_0 = (1 - \kappa)/\kappa\eta$                              |
| outer radius                                 | $R_2$                                       | $r_2 \equiv R_2/L_0 = (1 + \kappa)/\kappa\eta$                              |
| mean radius                                  | $\bar{R} \equiv (R_1 + R_2)/2$              | $\bar{r} \equiv (r_1 + r_2)/2 = 1/\kappa\eta$                               |
| duct width                                   | $\Delta R \equiv R_2 - R_1$                 | $\Delta r \equiv r_2 - r_1 = 2/\eta$  |
| permeability of vacuum                       | $\mu_0$                                     |   |
| viscosity coefficient                        | $\mu$                                       |   |
| density                                      | $\rho$                                      |   |
| electric conductivity                        | $\sigma$                                    |   |
| total current through the duct               | $I_0$                                       |   |
| strength of the impose axial magnetic field  | $B_0$                                       |   |
| scale of the velocity                        | $V_0 \equiv I_0/(4\pi L_0\sqrt{\sigma\mu})$ |   |
| scale of the current density                 | $J_0 \equiv I_0/(4\pi L_0^2)$               |   |
|  | field variables                             |   |
| radial coordinate                            | $R$   | $r \equiv R/L_0$  |
| axial coordinate                             | $Z$   | $z \equiv Z/L_0$  |
| vector of current density                    | $\mathbf{J}$                                | $\mathbf{j} \equiv \mathbf{J}/J_0$  |
| vector of induced magnetic field             | $\mathbf{B}$                                | $\mathbf{b} \equiv \mathbf{B}/(\mu_0 J_0 L_0)$                              |
| vector of velocity                           | $\mathbf{V}$                                | $\mathbf{v} \equiv \mathbf{V}/V_0$  |
| poloidal stream functions of velocity        |   | $w$   |
| angular momentum of the fluid                |   | $u \equiv rv_\theta$  |
| poloidal stream functions of current density |   | $h \equiv rb_\theta$  |
|  | characterized numbers                       |   |
| integrate-average azimuthal velocity         | $\bar{V} = V_0\bar{v}$                      | $\bar{v} \equiv \int_{-1}^1 \int_{r_1}^{r_2} v_\theta dr dz / 2(r_2 - r_1)$ |
| ratio of inner to outer radius               |   | $\kappa = (R_2 - R_1)/(R_1 + R_2)$  |
| ratio of height to width                     |   | $\eta = 2L_0/(R_2 - R_1)$   |
| Hartmann number                              |   | $M \equiv B_0 L_0 \sqrt{\sigma/\mu}$  |
| Reynolds number                              |   | $Re \equiv \rho V_0 L_0 / \mu$  |
| magnetic Reynolds number                     |   | $Re_m \equiv \mu_0 \sigma V_0 L_0$  |
| magnetic Prandtl number                      |   | $Pr_m \equiv \mu_0 \sigma \mu / \rho$                                       |

Table 1: Symbol notations.

where the differential operators are defined as:

$$f_1 \otimes f_2 \equiv \frac{\partial f_1}{\partial r} \frac{\partial f_2}{\partial z} - \frac{\partial f_1}{\partial z} \frac{\partial f_2}{\partial r}, \quad \Delta^* = \frac{\partial^2}{\partial r^2} - \frac{1}{r} \frac{\partial}{\partial r} + \frac{\partial^2}{\partial z^2} \quad (6a, b)$$

Hartmann number  $M$  and Reynolds number  $Re$ :

$$M \equiv B_0 L_0 \sqrt{\frac{\sigma}{\mu}}, \quad Re \equiv \frac{\rho V_0 L_0}{\mu} \quad (7a, b)$$

There are many parameters controlling the solution as listed in 1. But in nondimensional case, the parameters can be deduced into only two physical number, namely Hartmann number  $M$  and Reynolds number  $Re$ , and two geometric parameters of

$$\kappa \equiv \frac{R_2 - R_1}{R_2 + R_1}, \quad \eta \equiv \frac{2L_0}{R_2 - R_1} \quad (8a, b).$$

Specifically,  $\kappa$  measures the curvature of annular channel; when  $\kappa \rightarrow 0$ , the channel can be treated as a straight one.  $\eta$  refers to the ratio of height to width; the cross-section of channel is flat when  $\eta \ll 1$ , and tall when  $\eta \gg 1$ . The nondimensional length can be expressed by  $\kappa$  and  $\eta$ :  $r_1 = R_1/L_0 = (1 - \kappa)/\kappa\eta$ ,  $r_2 = R_2/L_0 = (1 + \kappa)/\kappa\eta$ . And the boundary conditions can be written as:

$$\begin{cases} r = (1 \pm \kappa)/\kappa\eta : & u = w = \partial_r w = 0, \quad \partial_r h = 0 \\ z = \pm 1 : & u = w = \partial_z w = 0, \quad h = \pm 1 \end{cases} \quad (9)$$

### 3 Semi-Analytical Algorithm

#### 3.1 Perturbation expansion of inertial force

Expand the field variables as the series of  $Re$ :

$$u = u_0 + u_1 Re + u_2 Re^2 + \dots u_n Re^n + \dots \quad (10a)$$

$$h = (z + h_0) + h_1 Re + h_2 Re^2 + \dots h_n Re^n + \dots \quad (10b)$$

$$w = w_0 + w_1 Re + w_2 Re^2 + \dots w_n Re^n + \dots \quad (10c)$$

We write  $z + h_0$  rather than  $h_0$  in equation 10b so that the boundary conditions of  $u_n, h_n, w_n$  are all homogeneous. Submitting the expansion form to the original equation 5 produce the equations regards to each power of  $Re$ :

$$Re^0 : \begin{cases} \begin{bmatrix} \Delta^* & M\partial_z \\ M\partial_z & \Delta^* \end{bmatrix} \begin{bmatrix} u_0 \\ h_0 \end{bmatrix} = \begin{bmatrix} -M \\ 0 \end{bmatrix} \\ w_0 = 0 \end{cases} \quad (11)$$

$$Re^1 : \begin{cases} u_1 = h_1 = 0 \\ (\Delta^* \Delta^* - M^2 \frac{\partial^2}{\partial z^2}) w_1 = \frac{1}{r^2} \frac{\partial u_0^2}{\partial z} \end{cases} \quad (12)$$

$$Re^2 : \begin{cases} \begin{bmatrix} \Delta^* & M\partial_z \\ M\partial_z & \Delta^* \end{bmatrix} \begin{bmatrix} u_2 \\ h_2 \end{bmatrix} = -\frac{1}{r} \begin{bmatrix} u_0 \otimes w_1 \\ 0 \end{bmatrix} \\ w_2 = 0 \end{cases} \quad (13)$$

We can solve  $u_0$  &  $h_0$ ,  $w_1$ ,  $u_2$  &  $h_2$  et al. in turn and write down more equations regards to higher power of  $Re$ . This process uncouples the primary flow  $u$  and secondary flow  $w$ , though the primary flow  $u$  is coupled with electromagnetic field  $h$ . In each term of  $Re$ , the original problem is transformed into the 2-order coupling PDEs for primary flow and electromagnetic field ( $u$  &  $h$  field):

$$\Delta^* u + M\partial_z h = S_w \quad (14a)$$

$$\Delta^* h + M\partial_z u = 0 \quad (14b)$$

and the 4-order PDE for secondary flow field ( $w$  field):

$$(\Delta^* \Delta^* - M^2 \partial_{zz}) w = S_u, \quad (15)$$

where the sources  $S_w$  and  $S_u$  on the right side are obtained via the term with lower-order  $Re$  as shown in equations 11, 12 and 13, and thus have been uncoupled with the left hand. With this perturbation expansion, we proceed to solve equations 14 and equation 15 in subsection 3.2 and 3.3, respectively.

#### 3.2 Spectral-Galerkin scheme for primary flow and electromagnetic field

We try to find the weak solution of equations 14 by the Galerkin approach based on spectral method, and set:

$$u = \sum_{n=1}^{\infty} u_{r,n}(r) u_{z,n}(z), \quad (16a)$$

$$h = \sum_{n=1}^{\infty} h_{r,n}(r) h_{z,n}(z) \quad (16b)$$

$u_{r,n}(r)$  and  $h_{r,n}(r)$  are spectral-Bessel functions determined by the left side of equation 14 as:

$$\frac{\partial^2 u_{r,n}}{\partial r^2} - \frac{1}{r} \frac{\partial u_{r,n}}{\partial r} = -\eta^2 \alpha_n^2 u_{r,n}, \quad \frac{\partial^2 h_{r,n}}{\partial r^2} - \frac{1}{r} \frac{\partial h_{r,n}}{\partial r} = -\eta^2 \beta_n^2 h_{r,n} \quad (17)$$

where  $\alpha_n$  and  $\beta_n$  are the eigenvalues. Appendix A shows the details for how  $u_{r,n}(r)$  and  $h_{r,n}(r)$  are deduced. Define the integral operator for arbitrary functions  $f_1$  and  $f_2$  as:

$$\langle f_1, f_2 \rangle \equiv \int_{r_1}^{r_2} f_1 f_2 \frac{1}{r} dr \quad (18)$$

The orthogonal law of Sturm-Liouville theory (Birkhoff and Merzbach, 1973) tells

$$\langle u_{r,i}, u_{r,j} \rangle = \langle h_{r,i}, h_{r,j} \rangle = \delta_{i,j}, \quad (19)$$

in which  $\delta$  is the Dirac function. With this orthogonality, integrating the product of  $u_{r,i}$  and equation 14a (the weight function is  $1/r$ ) (Duncan, 1848) we can obtain the weak-form of equation 14a

$$(u''_{z,i} - \eta^2 \alpha_i^2 u_{z,i}) + M \langle u_{r,i}, h_{r,j} \rangle h'_{z,j} = \langle S_w, u_{r,i} \rangle. \quad (20)$$

$i$  is a specific positive integer and  $j$  is supposed to follow Einstein summation convention. Similarly, weak-form of equation 14b is.

$$\langle u_{r,i}, h_{r,j} \rangle (h''_{z,j} - \eta^2 \beta_i^2 h_{z,j}) + M u'_{z,i} = 0 \quad (21)$$

At this point, the coupled two PDEs 14 has been reduced into a set of ODEs. The detailed solution to them is presented in Appendix B. It is noticed that the calculating cost has also been reduced dramatically compared with the common numerical scheme of finite difference, To be specific, if the  $n \times n$  resolution ( $n^2$  meshing points) is required, only the magnitude of  $n$  linear equations have to be solved by this spectral scheme, which takes on a global approach (Gottlieb and Orszag, 1977).

### 3.3 Pseudo-spectral scheme for secondary flow

We take the tentative weak solution to equation 5 as

$$w(r, z) = \sum_i \sum_j c_{i,j} w_{r,i}(r) w_{z,j}(z) \quad (22)$$

where  $w_{r,i}$  and  $w_{z,j}$  are the spectral functions, and  $c_{i,j}$  is undetermined coefficients. To meet the boundary condition 9, the radial spectral functions for  $w$  are of Bessel type as:

$$w_{r,i}(r) = (r - r_1)(r_2 - r) u_{r,i}(r) \quad (23)$$

and the axial spectral functions are chosen as:

$$w_{r,j}(z) = (1 - z^2) \sin(j\pi z) \quad (24)$$

Submitting the tentative solution 22 into the original equation 5 at the given grid, we obtain the linear equation set of  $c_{i,j}$ .

## 4 Results: Inertialess Regime

In inertialess regime, the secondary flow can be neglected and then the velocity is along the poloidal coordinate. This situation can exist in both high- $M$  or low- $M$  cases as long as  $Re$  is small enough as equation 5 implies. The equations of  $u$  &  $h$  field is:

$$\Delta^* u + M \partial_z h = 0 \quad (25a)$$

$$\Delta^* h + M \partial_z u = 0 \quad (25b)$$

accompanied by the boundary condition 9. And the final solution  $v(r, z)$  rests with  $\kappa$ ,  $\eta$ , and  $M$  exclusively. By virtue of the computationally cheap semi-analytical algorithm proposed in section 3, a large number ( $200 \times 200 = 40,000$ ) of cases are carried out in the whole parameter space spanned by  $\eta$  and  $M$ , each of which ranges from  $10^{-2}$  to  $10^2$ .

Before investigating the microcosmic flow structures, we view the macroscopic flow characters subjected to different Hartmann numbers and geometric parameters. The nondimensional integrate-average azimuthal velocity  $\bar{v}$  is used to verify solutions and classify flow patterns (Poyé et al., 2020):

$$\bar{v} = \frac{1}{2(r_1 - r_2)} \int_{-1}^1 \int_{r_1}^{r_2} v_{\theta} dr dz, \quad (26)$$

According to equation 26,  $\bar{v}$  is obtained by integrating the 2-dimensional azimuthal velocity  $v$  from the calculated cases with different  $\eta$  and  $M$ ; the results are presented in figure 2 (a). It is noticed that there are phenomenological areas with different variational trends in this  $\bar{v}$  contour figure. Interestingly, these areas can be well delimited by the red, blue, and green curves with special physical meanings. We name these areas a combination of capital letters C (coupled), D (decoupled), R (R-direction boundary layers), Z (Z-direction boundary layers) and N (no boundary layers). The principle of delimiting is as followings.

### 4.1 Division of flow patterns

#### 4.1.1 Electrically coupled modes

These areas in figure 2 (a) fall into two classes C-areas (coupled) and D-areas (decoupled) by the red curve. It can be seen in figure 2 (a) that D areas see symmetrical trends of  $\bar{v}$ , of which contours are controlled by  $\lg M \pm \lg \eta$ . By contrast, symmetry vanishes in C-areas where variation of  $\bar{v}$  with  $M$  levels off. Further study indicates that this discrepancy is

related to electrically coupling strength in the MHD system 25, namely the extent to which the flow field  $u$  disturbs the electromagnetic field  $h$ . The totally decoupled state that  $h$  is not influenced by  $u$ , corresponds to the case that  $M\partial_z u$  is negligible in equation 25b:

$$\frac{\partial^2 h}{\partial r^2} - \frac{1}{r} \frac{\partial h}{\partial r} + \frac{\partial^2 h}{\partial z^2} = 0 \quad (27)$$

Given boundary condition 9, equation 27 leads to a simple solution  $h(r, z) = z$ . To estimate the deviation from this decoupled state, we define the electrically coupling factor  $\epsilon$  as

$$\epsilon = \frac{\|h(r, z) - z\|}{\|z\|}, \quad (28)$$

where the energy norm operator is

$$\|f(r, z)\| \equiv \sqrt{\int_{-1}^1 \int_{r_1}^{r_2} f(r, z)^2 \frac{1}{r} dr dz}. \quad (29)$$

$\epsilon$  is calculated in  $\eta$ - $M$  space; results are shown in figure 2 (b). It can be seen that  $\epsilon$  has different scale laws at small  $\eta$  and large  $\eta$ . For an analytical investigative, taking the first two terms in semi-analytical operation 16 we can get a analytical approximate solution for  $h$ :

$$h = z - M^2 \frac{z - \operatorname{csch}(\sqrt{\alpha_1 \eta^2 + M^2}) \sinh(z \sqrt{\alpha_1 \eta^2 + M^2})}{\alpha_1 \eta^2 \sqrt{\alpha_1 \eta^2 + M^2} \coth(\sqrt{\alpha_1 \eta^2 + M^2}) + M^2}. \quad (30)$$

With the above analytical formula,  $\epsilon$  can be readily obtained:

$$\epsilon = \frac{M^2 \sqrt{\frac{6}{\alpha_1 \eta^2 + M^2} - \frac{9 \coth \sqrt{\alpha_1 \eta^2 + M^2}}{2 \sqrt{\alpha_1 \eta^2 + M^2}} - \frac{3}{2} \operatorname{csch}^2 \sqrt{\alpha_1 \eta^2 + M^2} + 1}}{\alpha_1 \eta^2 \sqrt{\alpha_1 \eta^2 + M^2} \coth \sqrt{\alpha_1 \eta^2 + M^2} + M^2} \quad (31)$$

Complex as this expression is, it is controlled by three parameters  $M$ ,  $\eta$  and  $\alpha_1$ .  $\kappa$  is involved in  $\epsilon$  through  $\alpha_1$ . However, mathematically,  $\alpha_1$  is the first eigenvalue ranging from  $\pi/2$  to 2, and thus has marginal effect on  $\epsilon$ . At this point,  $\kappa$ , namely the curvature of annular channel, can NOT determine the magnitude of electrically coupled factor  $\epsilon$ . By contrast, the effect of  $M$  and  $\eta$  is significant, as can be seen in both equation 31 and figure 2 b. Interestingly, the scale law of  $\epsilon$  vs.  $M$  is not obvious, but varies with  $\eta$ . When  $\eta \ll 1$  and  $M \ll 1$ , we have the Taylor's expansion for  $\epsilon$  as

$$\epsilon = \frac{1}{3} \sqrt{\frac{2}{35}} M^2 - \frac{13 \alpha_1 M^2}{45 \sqrt{70}} O(\eta^2) \approx \frac{1}{3} \sqrt{\frac{2}{35}} M^2, \quad (32)$$

therefore the contours of  $\epsilon$  is approximately horizontal when  $\eta \ll 1$  in  $M$ - $\eta$  space, as can be seen in figure 2 (b). When  $\eta \gg 1$ , the series is expanded as:

$$\epsilon = \frac{M/\eta^2}{\alpha_1 + M/\eta^2} - \frac{\alpha_1^2}{2(\alpha_1 + M/\eta^2)^2} O\left(\frac{1}{\eta^2}\right) \approx \frac{M/\eta^2}{\alpha_1 + M/\eta^2}, \quad (33)$$

therefore the slope of contours of  $\epsilon$  is approximately 2 when  $\eta \gg 1$  in  $M$ - $\eta$  space, as shown in figure 2 (b).

#### 4.1.2 Boundary layer modes

The flow patters can also be identified from the perspective of boundary layers. In this paper, the thickness of boundary layers are defined as the position where velocity reaches 95% of its maximum (this percentage can also be chosen as 90% or 99% without significantly different consequences). Figure 2 (c) and (d) depict the R-direction (radial) thickness of layers  $\delta_R$  and Z-direction (axial) thickness  $\delta_Z$ , respectively. Particularly, layers with  $\delta_R$  are adjacent to side walls while layers with  $\delta_Z$  are adjacent to end walls. They are modified by half of the radial dimension ( $\Delta R/2$ ) and half of the axial dimension ( $L$ ), respectively. Hence,  $\delta_R$  or  $\delta_Z \sim 1$  means the opposite layers overlap, in other words, there is no clear boundary layers along this direction. It is remarkable in figure 2 (c) and (d) that the thicknesses of boundary layers present distinct laws of variation in C-areas (above the red curve) and D-areas (below the red curve).

For the coupled case, the law of boundary layer is clearly understood by literature. Early, Shercliff and Batchelor (1953) employed the singular perturbation method to the MHD flow in straight channel with transverse magnetic fields.

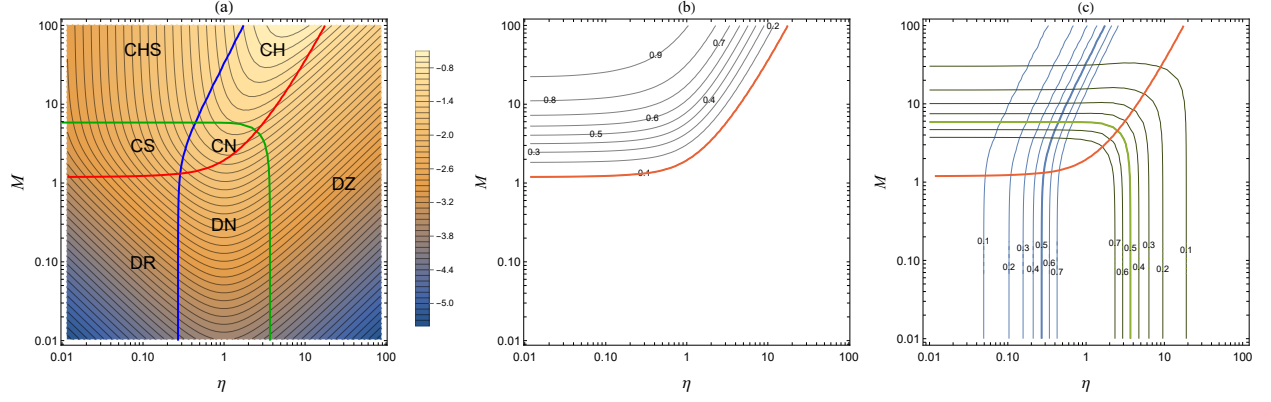


Figure 2: Contours in the  $\eta$ - $M$  space with  $\kappa = 1/9$ : (a) average velocity  $\bar{v}$ ; (b) electrically coupling factor  $\epsilon$ ; (c) thickness of boundary layer adjacent to side walls  $\delta_r$  (blue) and thickness of boundary layer adjacent to end walls  $\delta_z$  (green). The red thick curve in (a)&(b) ( $\epsilon = 0.1$ ) is the critical contour separating electrically coupled region (C-areas) and decoupled region (D-areas). The blue thick curve ( $\delta_r = 0.5$ ) and green thick curve ( $\delta_z = 0.5$ ) in (a)&(c) are demarcation of regions with clear boundary layers.

They identified there were Shercliff layers adjacent to conductive walls with thickness of  $1/\sqrt{M}$  and Hartmann layers adjacent to insulative walls with thickness of  $1/M$  under strong magnetic fields. The layer thickness criteria were later validated and adopted in annular cases (Baylis and Hunt, 1971; Tabeling and Chabrierie, 1981; Khalzov et al., 2010). Considering that the nondimensional scales of radial and axial length of channel are  $\sim 1/\eta$  and  $\sim 1$ , respectively, the modified thickness shall be

$$\delta_R \sim \eta/\sqrt{M}, \quad (34a)$$

$$\delta_Z \sim 1/M. \quad (34b)$$

These two formulas can well explain the diagonal blue line and horizontal green line in figure 2 (c), respectively.

For the decoupled case, little previous research is available. Since  $h = z$  is accepted in the decoupled case, the equation of  $u$  can be reduced to

$$\frac{\partial^2 u}{\partial r^2} - \frac{1}{r} \frac{\partial u}{\partial r} + \frac{\partial^2 u}{\partial z^2} + M = 0 \quad (35)$$

A closer view to the equation shows that Hartmann number  $M$  do not influence the flow field structure, but merely scales up the magnitude of velocity. That account for the vertical contours of thickness in  $M$ - $\eta$  space in figure 2 (c). To clarify the effect of  $\eta$ , we set  $x = r\eta$  so that the boundary conditions  $x = (1 \pm \kappa)/\kappa$  are free of  $\eta$ , and then get:

$$\eta^2 \left( \frac{\partial^2 u}{\partial x^2} - \frac{1}{x} \frac{\partial u}{\partial x} \right) + \frac{\partial^2 u}{\partial z^2} + M = 0 \quad (36)$$

The scale laws of thickness of boundary layer can be easily acquired from the above equation: when  $\delta_R$  exists, the scales within radial layers are

$$\eta^2 \left( \frac{\partial^2 u}{\partial x^2} - \frac{1}{x} \frac{\partial u}{\partial x} \right) \sim \frac{\eta^2 u}{\delta_R^2}, \quad \frac{\partial^2 u}{\partial z^2} \sim u, \quad \text{thus } \delta_R \sim \eta; \quad (37)$$

when  $\delta_Z$  exists, the scales within axial layers are

$$\eta^2 \left( \frac{\partial^2 u}{\partial x^2} - \frac{1}{x} \frac{\partial u}{\partial x} \right) \sim \eta^2 u, \quad \frac{\partial^2 u}{\partial z^2} \sim \frac{u}{\delta_Z^2}, \quad \text{thus } \delta_Z \sim \frac{1}{\eta}. \quad (38)$$

The scale laws  $\delta_R \sim \eta$  and  $\delta_Z \sim 1/\eta$  account for the symmetry of contours of  $\delta_R$  and  $\delta_Z$  in  $M$ - $\eta$  space as can be seen in figure 2 (c).

These ‘boundary layers’ in decoupled mode is fundamentally different from those in coupled mode. The latter is caused by  $M$  in magnetohydrodynamic context, while the former can be considered as a hydrodynamic profile stretched by coordinates.



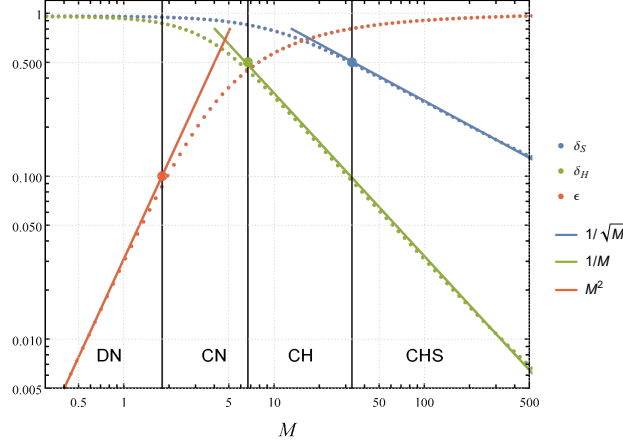


Figure 3: Variations of the electrically coupling factor  $\epsilon$  and the thickness of boundary layers  $\delta_r$  and  $\delta_r$  with increasing  $M$  at  $\eta = 1, \kappa = 1/9$ . The dots are semi-analytical solution, while red, blue and green lines come from analytical theories 32 and 34 (a) and 34 (b) respectively. The large points and plumb black lines mark the demarcations between different patterns.

### 4.1.3 Analysis of criticality

The red, blue and green curves, which divide areas in figure 2 (a), are  $\epsilon = 0.1$  contour in (b) and  $\delta_R = 0.5, \delta_Z = 0.5$  contours in (c), respectively. Although 0.1 and 0.5 are not exactly-obtained numerical indicators, these separating curves are not arbitrary at all. Firstly, in terms of the red curve, as can be seen in figure 2 (c), the contours of  $\delta_R$  and  $\delta_Z$  see clear transition in the vicinity of  $\epsilon = 0.1$  contour. Secondly, in terms of the blue and green curves, the contours of  $\delta_R = 0.5$  and  $\delta_Z = 0.5$  can well divide the contours of  $\epsilon$  into horizontal, crooked and sloping section. Finally, we depict the variation of  $\epsilon, \delta_Z, \delta_R$  with  $M$  at  $\eta = 1$  in figure 3. This figure illustrates that with the increase of  $M$ ,  $\epsilon$  (red dots) deviate from  $\sim M^2$  law (red line) indicated by equation 32 in the vicinity of  $\epsilon = 1$  (red points), after which the increasing trend show clear transition;  $\delta_Z$  (green dots) enter the regime of  $\sim 1/M$  (green line) indicated by equation 34 (a) in the vicinity of  $\delta_Z = 0.5$  (green points);  $\delta_R$  (blue dots) enter the regime of  $\sim 1/\sqrt{M}$  (blue line) indicated by equation 34 (b) in the vicinity of  $\delta_R = 0.5$  (green points). In that context, it is reasonable to select these demarcation curves separating different areas.

## 4.2 Analytical theory for flow patterns

This section is devoted to the comprehensive analytical study on flow patterns in inertialess regime. We will summarize previous analytical theory or develop new ones for each pattern.

Figure 4 illustrates the velocity and current stream of 4 patterns in coupled mode in C-areas. For these patterns, the coupling between flow field and electric field must be concerned according to equation 25.

- **CRZ Pattern:** In CRZ pattern, flow profile shows the boundary layers in both R direction and Z direction. This pattern only exists at  $M \gg 1$  and  $\sqrt{M} \gg \eta$  as equation 34 indicates, in other words, above the blue and green curves figure 2 (a). A representative case with  $\eta = 1$  and  $M = 80$  in CRZ area is examined. Contours of modified velocity  $v/v_{\max}$  ( $v_{\max}$  is the peak of  $v$ ) and current stream  $h$  are shown in figure 4 (a) and (d), respectively. The Hartmann layers adjacent to end walls and Shercliff layers adjacent to side walls coexist in the velocity field. Besides, the current stream field also see the concentration within Hartmann layers region, and great bend near Shercliff layers region. This structure, which is solved out by our spectral method, is in good agreement with the numerical simulations of Khalzov et al. (2010) and Zhao and Zikanov (2012). In terms of  $\bar{v}$  law of CRZ pattern, Baylis and Hunt (1971) employed boundary layer analysis method and obtained the analytical formula:

$$\bar{v} = \frac{\eta}{2} \ln \left( \frac{1+\kappa}{1-\kappa} \right) \left( 1 - \frac{1.912\eta\kappa}{\sqrt{M}(1-\kappa^2) \ln \left( \frac{1+\kappa}{1-\kappa} \right)} + O\left(\frac{1}{M}\right) \right) \quad (39)$$

This formula implicates that  $\bar{v}$  is free of  $M$  when  $M$  is large, which explain the almost upright contours shown in CRZ area of figure 2 (a).

- **CZ Pattern** Above the blue curve but below green curve in figure 2 (a) is CZ pattern, in which  $M \gg 1$  but  $\sqrt{M} \sim \eta$ . A representative case with  $\eta = 5$  and  $M = 80$  is examined. Contours of modified velocity  $v/v_{\max}$  and current stream  $h$  are shown in figure 4 (b) and (f), respectively. As expected, Hartmann layers exist in the velocity field while Shercliff layers vanish. Figure 4 (f) shows the current stream is squeezed near the end walls, but less bent near the side walls compared to the CRZ case shown in figure 4 (e). Using axial-force averaging with Hartmann layers present, Poth erat et al. (2000) created the model for radial profile of velocity with transverse magnetic field:

$$\frac{\partial^2 u}{\partial r^2} - \frac{1}{r} \frac{\partial u}{\partial r} - Mu + M = 0 \quad (40)$$

which is applicable in CZ pattern (Khalzov et al., 2010). The exact solution is a combination of 1-order modified Bessel functions  $I_1$  and  $K_1$ :

$$u(r) = 1 + C_1 r I_1(\sqrt{M}r) + C_2 r K_1(\sqrt{M}r), \quad (41)$$

where  $C_1$  and  $C_2$  are constants satisfying boundary conditions. It leads to the analytical formula for average velocity:

$$\bar{v} = 1 + \left( C_1 \left( I_0(\sqrt{M} \frac{1+\kappa}{\kappa\eta}) - I_0(\sqrt{M} \frac{1-\kappa}{\kappa\eta}) \right) + C_2 \left( K_0(\sqrt{M} \frac{1-\kappa}{\kappa\eta}) - K_0(\sqrt{M} \frac{1+\kappa}{\kappa\eta}) \right) \right) / \log\left(\frac{1+\kappa}{1-\kappa}\right) \quad (42)$$

- **CR Pattern** The case opposite to CZ pattern is called CR pattern, which is expected to occur when  $\sqrt{M} \gg \eta$  but  $M \sim 1$ . The representative calculating case of  $v/v_{\max}$  and  $h$  with  $\eta = 0.1$  and  $M = 3$  is presented in figure 4 (c) and (g). Figure 4 (c) shows that along radial axis velocity soars within Shercliff layers, while Hartmann layers are invisible. Contrary to CZ pattern in figure 4 (f), the current stream shown in (g) see clear bend near side walls but its axial distribution is relative even. The analytical theory for CR pattern will be established for the first time as followings. Beyond Shercliff layers, equations 25 should be transformed into:

$$\frac{\partial^2 u}{\partial z^2} + M \frac{\partial h}{\partial z} = 0, \quad u|_{z=\pm 1} = 0 \quad (43a)$$

$$\frac{\partial^2 h}{\partial z^2} + M \frac{\partial u}{\partial z} = 0, \quad h|_{z=\pm 1} = \mp 1 \quad (43b)$$

leading to solutions:

$$u_c = \coth(M) - \operatorname{csch}(M) \cosh(Mz) \quad (44a)$$

$$h_c = \operatorname{csch}(M) \sinh(Mz). \quad (44b)$$

Then the average velocity is:

$$\bar{v} = \frac{M \coth(M) - 1}{2M} \eta \ln \left( \frac{\kappa + 1}{1 - \kappa} \right) \quad (45)$$

- **CN Pattern** The case with  $\sqrt{M} \sim \eta$  and  $M \sim 1$  (corresponding to the area below blue curve and green curve but above red curve) is called CN pattern, in which no boundary layer shows up but the flow is still electrically coupled. The representative calculating case of  $v/v_{\max}$  and  $h$  with  $\eta = 1$  and  $M = 3$  is presented in figure 4 (d) and (h). The contours of velocity seem to be concentric circles; the current stream is slightly bent the channel, which differ from the decoupled case of  $h = z$ . 1-D analytical models will fail to depict this pattern. Nevertheless, since the high order terms in semi-analytical operation 16 contribute to the surge within boundary layers, we believe the truncation can produce a approximate solution to CN pattern without boundary layers. Appendix C discusses the convergence in details. In fact, for the case of  $\eta \sim 1$  and  $M \sim 1$ , the blue point in figure12 shows that the first term can constitute about more than 90% of the sum of series. With the truncation, the semi-analytical solution degenerate into a purely analytical one as:

$$v = \frac{\langle g_1, 1 \rangle}{\langle g_1, g_1 \rangle} \frac{1 - \frac{\cosh(z\sqrt{\alpha_1\eta^2+M^2})}{\cosh(\sqrt{\alpha_1\eta^2+M^2})}}{\alpha_1 \frac{\eta}{M} + \frac{M}{\eta} \frac{\tanh(\sqrt{\alpha_1\eta^2+M^2})}{\sqrt{\alpha_1\eta^2+M^2}}} \left( \frac{J_1(\alpha_1\eta r)}{J_1(\alpha_1 \frac{1+\kappa}{\kappa})} - \frac{Y_1(\alpha_1\eta r)}{Y_1(\alpha_1 \frac{1+\kappa}{\kappa})} \right) \quad (46)$$

Figure 5 illustrates the velocity and current stream of 3 patterns in decoupled mode in D-areas. Interestingly, in terms of the flow fields, DZ, DR, DN patterns are similar to CZ, CR, CN, respectively. The reason is that their boundary layers are similar, no matter whether  $\eta$  or  $M$  brings about these layers. The major difference is that the current stream in D-mode are all identical to  $h = z$  as shown in figure 5 (d), while the counterpart in C-mode show various twists or squeeze as can be seen in figure 4 (e)-(h). For these patterns in D-areas, the electric field is decoupled from flow field and the equation 36 shall be employed.

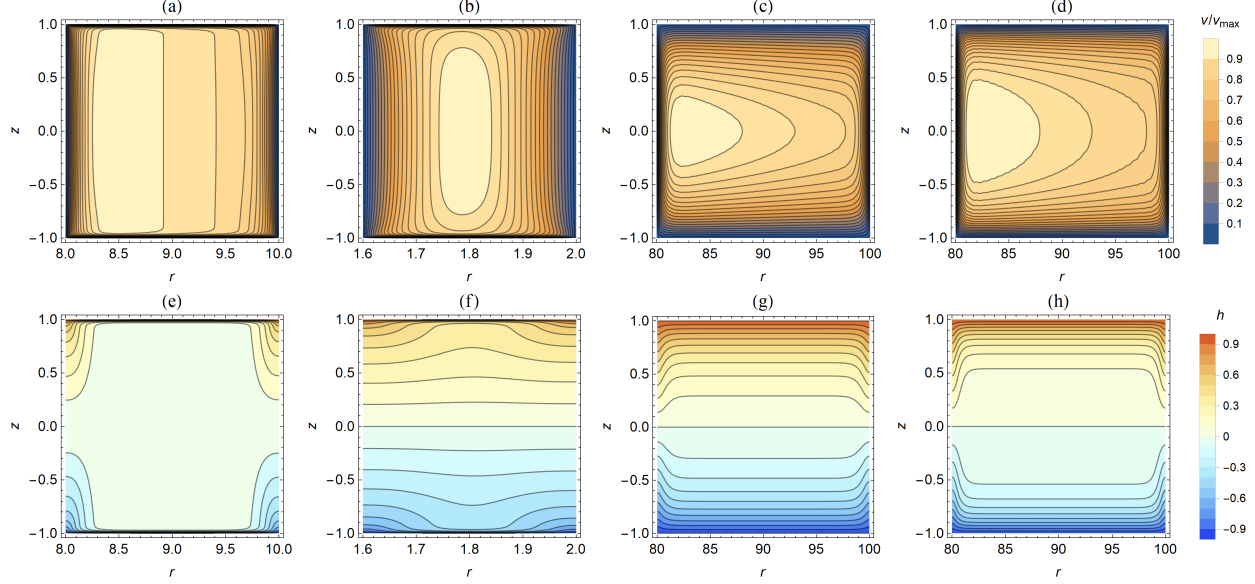


Figure 4: Top row: contours of the modified velocity  $v/v_{\max}$ ; bottom row: current stream  $h$  in coupled mode. first column:  $\eta = 1, M = 80$  in CRZ area; second column:  $\eta = 5, M = 80$  in CZ area; third column:  $\eta = 0.1, M = 3$  in CR area; fourth column:  $\eta = 1, M = 3$  in CN area.

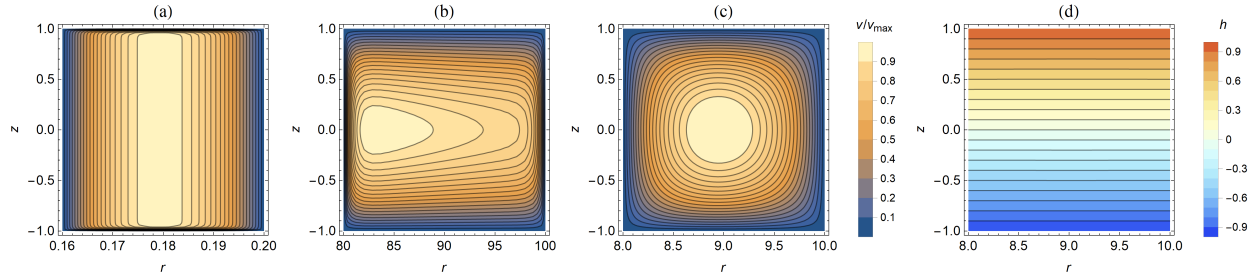


Figure 5: Contours of modified velocity  $v/\bar{v}$  of (a):  $\eta = 50, M = 1$  in DZ area; (b):  $\eta = 0.1, M = 0.1$  in DR area; (c):  $\eta = 1, M = 0.1$  in DN area; and (d) contours of current stream  $h$  in decoupled regions

- **DZ pattern** When  $\eta \gg 1$  and  $M \ll \eta^2/\alpha_1$  (as indicated by equation 33), flow profile falls in DZ pattern. A representative case with  $\eta = 50$  and  $M = 1$  in DZ area is examined in figure 5 (a). Beyond the Z-direction boundary layers, equation 36 is reduced to

$$\eta^2 \left( \frac{\partial^2 u}{\partial x^2} - \frac{1}{x} \frac{\partial u}{\partial x} \right) + M = 0, \quad x = \eta r \quad (47)$$

Its analytical solution is:

$$u = M \frac{(\kappa^2 - 1)^2}{\eta^2 \kappa^3} \ln \left( \frac{1 - \kappa}{\kappa + 1} \right) + r^2 \ln \left( \frac{(\kappa + 1)^{\frac{(\kappa+1)^2}{\kappa}} (1 - \kappa)^{\frac{(\kappa-1)^2}{-\kappa}}}{(\eta \kappa)^4 r^4} \right), \quad (48)$$

and average velocity is

$$\bar{v} = M \frac{\kappa^2 - (\kappa^2 - 1)^2 \operatorname{arctanh}^2(\kappa)}{4\eta \kappa^3} \sim \frac{\kappa M}{3\eta} + O(\kappa^3). \quad (49)$$

This final formula implicates the slope of  $\bar{v}$  contours in  $M$ - $\eta$  space is  $-1$ , as figure 2 (a) exactly shows.

- **DR pattern** When  $\eta \ll 1$  and  $M \ll 1$  (as indicated by equation 32), flow profile falls in DR pattern. A representative case with  $\eta = 1$  and  $M = 0.1$  in DR area is examined in figure 5 (b). Beyond the R-direction

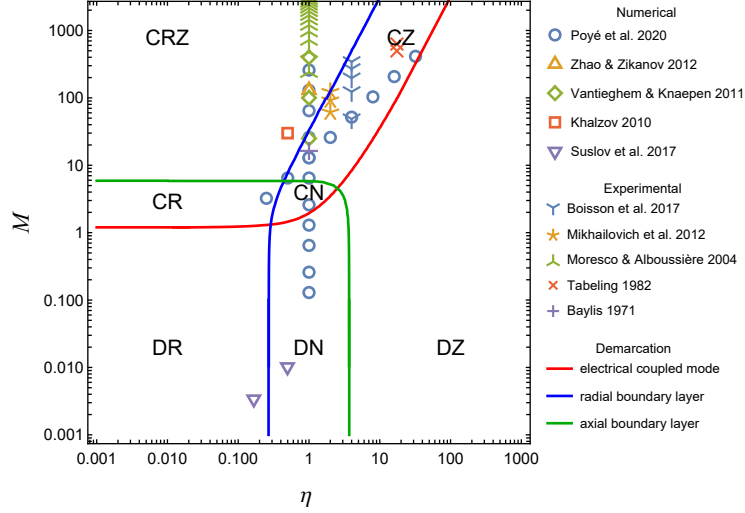


Figure 6: Flow patterns in inertial regime. The hollow markers, asterisks, coloured areas represent previous numerical, experimental and analytical studies respectively.

boundary layers, equation 36 is reduced to

$$\frac{\partial^2 u}{\partial z^2} + M = 0, \quad (50)$$

leading to a simple solution for  $u$  and  $\bar{v}$

$$u = M(1 - z^2)/2, \quad (51)$$

$$\bar{v} = \frac{1}{6}\eta M \log\left(\frac{\kappa + 1}{1 - \kappa}\right), \quad (52)$$

which indicates the slope of  $\bar{v}$  contours in  $M$ - $\eta$  space is 1, as figure 2 (a) exactly shows.

- **DN pattern** When  $\eta$  is moderate, there are not any boundary layers in decoupling mode regards to DN area. A representative case with  $\eta = 1$  and  $M = 0.1$  in DN area is examined in figure 5 (c). Similar to CN pattern, 2-D effect must be considered. We solve the decoupled equation 36 by the method of variable separating and obtain:

$$u(r, z) = M \sum_{i=1}^{\infty} \frac{\langle u_{r,i}, 1 \rangle}{\eta^2 \alpha_i^2} u_{r,i}(r) \left(1 - \frac{\cosh(\eta \alpha_i z)}{\cosh(\eta \alpha_i)}\right) \quad (53)$$

With this series solution, we can figure out the average velocity:

$$\bar{v} = M \sum_{i=1}^{\infty} \frac{\langle u_{r,i}, 1 \rangle^2}{2\alpha_i^2} \left(1 - \frac{\tanh(\eta \alpha_i)}{\eta \alpha_i}\right) \frac{1}{\eta} \quad (54)$$

On the same ground with CN pattern, the first-order approach can be taken as:

$$\bar{v} \sim \left(1 - \frac{\tanh(\eta \alpha_1)}{\eta \alpha_1}\right) \frac{M}{\eta} \quad (55)$$

### 4.3 Applicability of semi-analytical solution

Figure 6 summarizes this current work together with previous investigations. The hollow markers and asterisks are previous numerical and experimental studies, respectively. It is noticed that previous work focused mainly on the CRZ and CZ patterns in a square cross-section with  $\eta = 1$ . Indeed, previous simulations were in principle also able to be applied for any single points in  $M$ - $\eta$  space. The semi-analytical solution proposed in this paper is supposed to recover previous data, and more importantly, cover all areas in the whole parameter space once and for all.

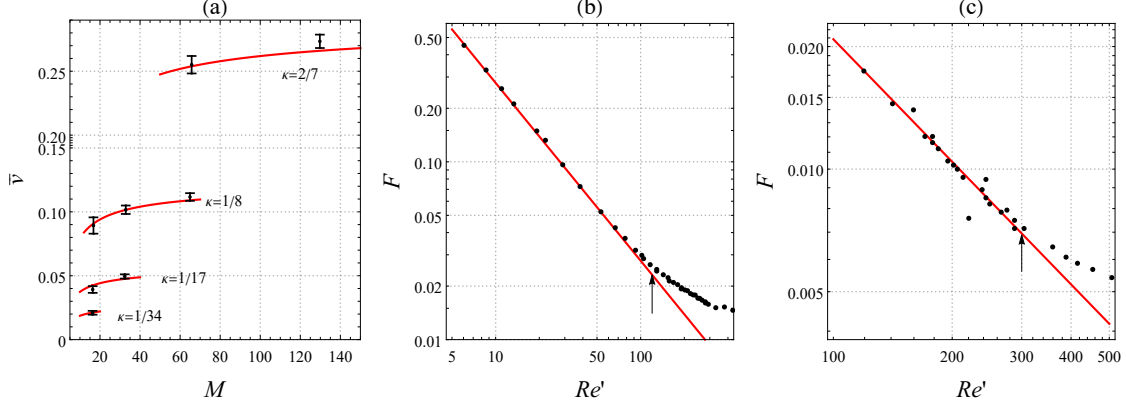


Figure 7: comparison between spectral solution (red curve) and experiment data (black points). (a) variations of  $\bar{v}$  with Hartmann number  $M$  at  $\eta = 1$  and  $\kappa = 1/34, 1/17, 1/8, 2/7$  compared with (Baylis and Hunt, 1971). (b) Friction factor  $F$  vs  $Re'$  compared with (Baylis, 1971). (c) Friction factor  $F$  vs  $Re'$  compared with (Moresco and Alboussi re, 2004). The arrows in (b) and (c) indicate transition points from laminar flow to turbulence.

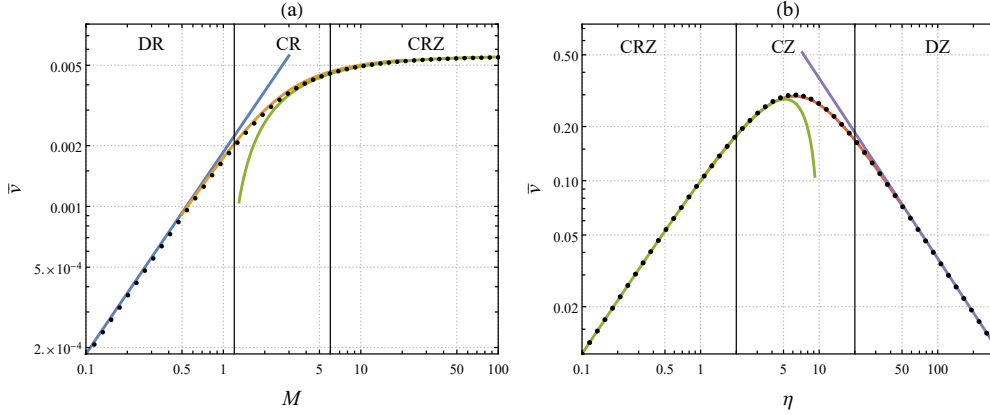


Figure 8: Comparison between spectral solution (black dots) and analytical theory (coloured lines: equation 52 (blue), equation 45 (yellow), equation 39 (green), equation 42 (red), equation 49 (purple)). (a) Variations of  $\bar{v}$  with Hartmann number  $M$  across DR, CS, and CRZ regions when  $\eta = 0.05$ . (b) Variations of  $\bar{v}$  with geometric ratio  $\eta$  across CRZ, CH, and DZ regions when  $M = 100$ .

The present semi-analytical solution is verified by the comparison with experiment data and analytical theory. On the one hand, there is amount of experiment data in CRZ region with great  $M$  and square section ( $\eta = 1$ ). The comparison between spectral solution and experiment in CRZ region is shown in figure 7. Figure 7(a) compared the variations of  $\bar{v}$  with Hartmann number  $M$  and  $\kappa$  obtained by spectral solution and Baylis and Hunt (1971) experiment. The growing tendency of  $\bar{v}$  with increasing  $M$  and  $\kappa$  coincides with experiment considering error bars. Another important parameter, friction factor which is defined as

$$F = \frac{I_0 B_0}{2\pi\rho\bar{R}(V_0\bar{v})^2} = \frac{M}{Re} \frac{2\kappa\eta}{\bar{v}}, \quad (56)$$

is concerned by the experiment of Baylis (1971) and Moresco and Alboussi re (2004). The relationship of  $F$  vs.  $Re'$ , where  $Re' = Re/M$ , is commonly used to detect transition from laminar flow to turbulence. Figure 7(b) and (c) compared this relationship calculated by the semi-analytic spectral solution and that measured by experiments. Note that the semi-analytic algorithm is based on laminar theory, while these experiments detected the transition from laminar flow to turbulence in the inertialess regime. The clear deviation between red curve and black points is therefore seen in figure 7(b) and (c), in spite of the good agreement before transition point labelled by the arrows.

On the other hand, the spectral solution can be verified by the analytical theory 39 for CRZ pattern, equation 42 for CZ pattern, equation 45 for CR pattern, equation 52 for DR pattern, and equation 49 for DZ pattern. Figure 8(a) shows  $\bar{v}$  vs.  $M$  with  $\eta = 0.05$ . It is noticed that scale laws of  $\bar{v}$  vary with Hartmann number  $M$ . To be specific, when  $M$  is small

(DR pattern), a clear linear relationship between  $\lg \bar{v}$  and  $\lg M$  can be seen as depicted by the blue line according to analytical approach 52. When  $M$  is large (CRZ pattern), the scale of  $\bar{v}$  is insensitive to the increase in  $M$  as depicted by the green curve according to analytical approach 39. However, both equation 39 and 52 fail in the transition zone (CR pattern), where the preciser analytical theory 45 (yellow curve) works. Figure 8(b) shows  $\bar{v}$  vs.  $\eta$  with  $M = 100$ . The scale of  $\bar{v}$  has a peak value in the proximity of  $\eta = 6$ , before which there is the linear increase in  $\lg \bar{v}$  as controlled by CRZ theory 39. Inversely, if  $\eta$  rises into DZ region,  $\lg \bar{v}$  will see a linear decline as depicted by the purple line of analytical theory 49. Similar to the case shown in (a), both equation 39 and 52 fail in the transition zone (CZ pattern), where another preciser analytical theory 42 (red curve) works.

It is an important identification that our semi-analytic results (black plus signs) coincide exactly with the specific analytical theory across all the six patterns with smooth transition.

## 5 Results: Inertial Regime

In inertial regime, the secondary flow and its effect on primary flow must be concerned. According to the perturbation expansion 10 described in section 3, we express  $u$  and  $w$  as the series of  $Re$ . Appendix D is devoted to the estimation of convergence of the series. Interestingly, the mathematical analysis tells that the convergence rests with  $Re' = Re/M$  instead of  $Re$ . This  $Re'$  is exactly the variable indicating the transition from laminar to turbulence (Moresco and Alboussière, 2004). The estimation we draw in Appendix D shows the convergence domain is about  $Re' < \kappa^{-2.5}$  ( $= 243$  in the case with  $\kappa = 1/9$ ). This convergence domain is slightly less than the transition point, at  $Re' \approx 380$ , in the experiment of Moresco and Alboussière (2004). Because the current research focuses on the laminar case, the convergence domain

$$Re' < \kappa^{-2.5} \quad (57)$$

is a conservative estimate for the applicability of the proposed perturbation method. Moreover, it is noticed that the even orders of  $Re$  vanish in the series for  $u$  while odd orders vanish in the series for  $w$  equations 10:

$$u = u_0 + u_2 Re^2 + u_4 Re^4 + \dots \quad (58)$$

$$w = w_1 Re + w_3 Re^3 + \dots \quad (59)$$

The scale analysis shows that:

$$\frac{u_4 Re^4}{u_2 Re^2} \sim \frac{w_3 Re^3}{w_1 Re} \sim \kappa^5 Re^2 \quad (60)$$

In the case of  $\kappa^5 Re^2 \ll 1$ , which can be reached easily at small  $\kappa$ , truncating the series is reasonable for examining the effect of  $Re$ :

$$u = u_0 + u_2 Re^2 \quad (61)$$

$$w = w_1 Re \quad (62)$$

The following results are calculated with fixed geometric parameter  $\eta = 1$  and  $\kappa = 1/9$ , which are the same as the investigation of Moresco and Alboussière (2004); Zhao and Zikanov (2012); Vantighem and Knaepen (2011).

Again, we must **emphasize** that there is no restriction on the magnitudes of  $Re$  nor  $M$  per se. As long as  $Re'$  is not too great, the flow remains laminar (Moresco and Alboussière, 2004), and the proposed perturbation solutions always converge.

### 5.1 evolution of secondary flow

Figure 9 (a)-(h) list the stream function  $w_1$  of secondary flow on the top row, and velocity perturbation  $v_2 = u_2/r$  due to inertial effect on the bottom row with incremental  $M$  from left to right. Note that  $v_2$  and  $w_1$  are not controlled by  $Re$  according to equation 61. This subsection is devoted to the structure of flow field and the magnitude will be discussed in the next subsection.  $w$  and  $v_2$  in figure 9 is normalized by the maximum and thus range from  $-1$  to  $1$ . It can be seen that the flow profiles vary with  $M$  and there are four different patterns, which are named oval, trapezoid, cracking, and separation patterns based on shape of secondary vortexes.

- **Oval pattern** Figure 9(a) and (e) depict the inertial case with  $M \sim 1$  corresponding to DN pattern in inertialess regime. Figure 9(a) shows a pair of oval antisymmetry secondary vortexes. Then the two large secondary vortexes modify the profile of primary flow via Ekman pump effect, enhancing azimuthal velocity on the outer side and weaken that on the inner, as shown in figure 9(e).

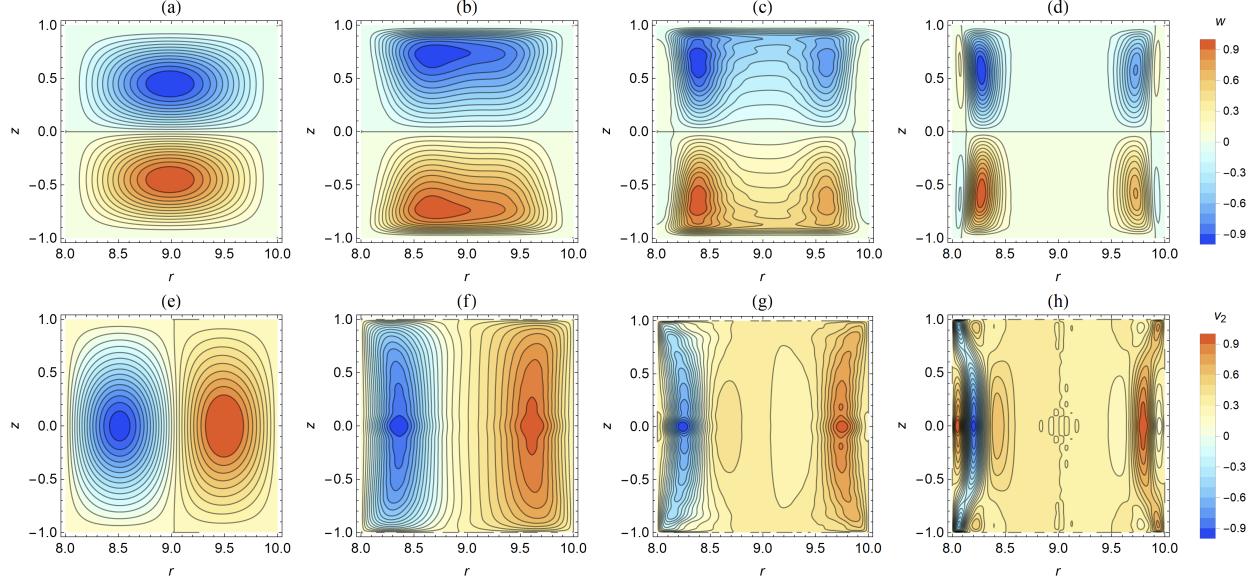


Figure 9: Top row: stream function  $w_1$  for secondary flow; bottom row: perturbation velocity  $v_2$  driven by inertial effect. First column:  $M = 1$ ; second column:  $M = 20$ ; third column:  $M = 50$ ; forth column:  $M = 100$ ;

- **Trapezoid pattern** Figure 9(b) and (f) depict the inertial case with  $M \sim 10$  corresponding to CZ pattern in inertialess regime. For the primary flow, Hartmann layers emerge near the insulation end walls. The rapid change in primary flow near Hartmann layers leads to the dramatic variation in  $v_r$  of secondary flow near the plate ends, as indicated by high density of contours in figure 9(b). The antisymmetry secondary vortices transformed into trapezoid, which coincides with the simulations of Vantieghe and Knaepen (2011). The perturbation velocity  $v_2$  stretches axially and has radial one-dimensional profile in the core region as can be seen in figure figure 9(f).
- **Cracking pattern** As Hartmann number goes up to  $M \sim 50$ , the trapezoid vortices have begun to crack and given birth to a second small peak near the outer side as shown in figure 9(c). This cracking phenomenon agree with the simulations of Zhao and Zikanov (2012). Note that reverse vortices adjacent to conductive torus walls also emerge along with the main vortices cracking. The reverse vortices can be identified by the separated zero-contours near radial boundaries and we will discuss their critical emergence later. And in this pattern, figure 9(g) shows that the perturbation velocity  $v_2$  is crushed radially resulting in dramatic perturbation near the torus surfaces but marginal effect in the middle region. Figure 9(g) can explain the results of Zhao and Zikanov (2012): inertial effect thicken inner Shercliff layer while thin outer Shercliff layer.
- **Separation pattern** When Hartmann number is large ( $M \sim 100$ ), the main vortices are broken into two separated parts and reverse vortices are fully developed as shown in figure 9(d). The anomalous reverse vortices conform the theoretical prediction of Tabeling and Chabrierie (1981). It can be seen in figure 9(h) that  $v_2$  has a drastic change from positive to negative within Shercliff layers. In this context, inertial effect can strengthen primary velocity near the inner side, which is opposite to other patterns stated before. This anomaly can be understood through the reverse vortices. According to equation 5 and the perturbation expansion in section 3, the equation for  $v_2$  can be expressed as:

$$0 = \Delta^*(rv_2) + M \frac{\partial h_2}{\partial z} + \frac{1}{r} \left( \frac{\partial u_0}{\partial r} \frac{\partial w_1}{\partial z} - \frac{\partial u_0}{\partial z} \frac{\partial w_1}{\partial r} \right) \quad (63)$$

Note that  $\partial_r u$  is great within Shercliff layers when  $M$  is large. And the reverse vortices of secondary flow raise the dramatic signed shift of  $\partial_z w$  along the middle axis  $z = 0$  near Shercliff layers. Hence, there is the reversal sign in source item  $\partial_r u \partial_z w$ , which leads to the anomalous inertial perturbation on primary flow.

## 5.2 scale formula of suppression of inertial effect

We define  $E$  to estimate the scale of inertial effect:

$$E = \bar{R}e^2 \frac{\|v_2\|}{\|v_0\|}, \quad (64)$$

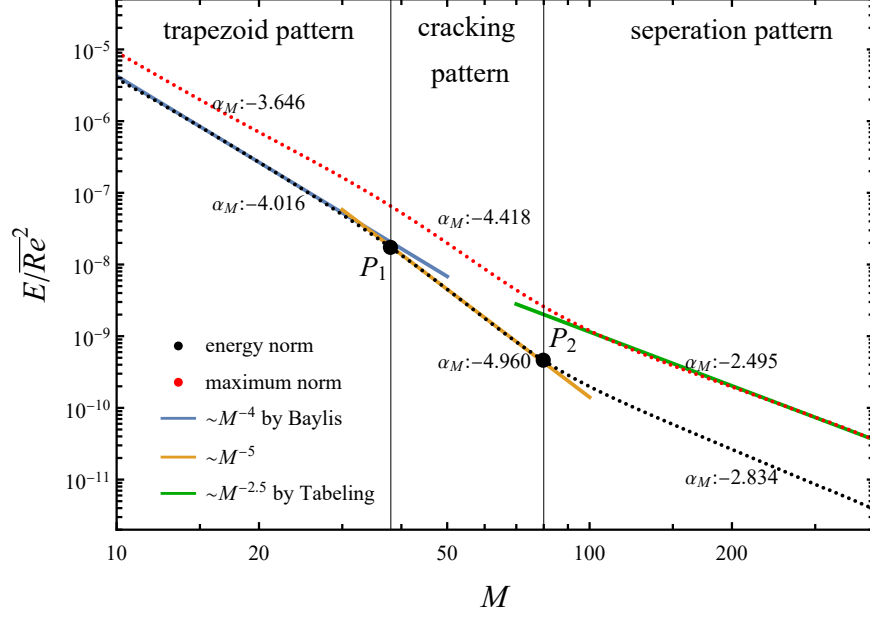


Figure 10: Scale of inertial perturbation on primary velocity. Black and red points are spectral results according to equation 64 and equation 65, respectively. Blue line are  $\alpha_M = -4$  theory of Baylis and Hunt (1971); green line is  $\alpha_M = -2.5$  theory of Tabeling and Chabrerie (1981); yellow line with  $\alpha_M = -5$ . All the label  $\alpha_M : XXX$  comes from local linear fitting for the energy norm or maximum norm.

where  $\bar{Re} = v_0 Re$  is spatially average Reynolds number,  $\|f\|$  is the energy norm defined in equation 29. The norm operator is not one and only. The maximum norm can also be used:

$$E = \bar{Re}^2 \frac{\max\{v_2\}}{\max\{v_0\}}, \quad (65)$$

There is no final conclusion about which norm operator is better to estimate the scale of inertial effect. The contribution of Reynolds number to inertial effect is clear as  $E \sim \bar{Re}^2$ , while the effect of Hartmann number is latent. Based on scale analysis of Hartmann layers, the theory of Baylis and Hunt (1971) declare:

$$E \sim \bar{Re}^2 / M^4. \quad (66)$$

By contrast, based on scale analysis of Shercliff layers, the theory of Tabeling and Chabrerie (1981) declare:

$$E \sim \bar{Re}^2 / M^{2.5} \quad (67)$$

In order to examine the index of Hartmann number

$$\alpha_M = \frac{\partial \lg E / \bar{Re}^2}{\partial \lg M}, \quad (68)$$

figure 10 presents  $E/\bar{Re}^2$  vs.  $M$  in logarithmic plot. 120 cases with different  $M$  are calculated in this inertial regime. The black points are calculated by equation 64 based on  $v_2$  and  $v_0$  results. Blue and green lines refer to energy norm 66 and maximum norm 67, respectively. It can be seen that the increasing  $M$  suppresses the magnitude of inertial perturbation. The spectral results agree with  $M^{-4}$  theory when  $M < 40$  (before  $P_1$ ), but drop faster than  $M^{-4}$  when  $40 < M < 80$  (between  $P_1$  and  $P_2$ ). The linear fitting of spectral results gives the relationship of  $\sim M^{-5}$ . When  $M > 80$ , the suppression effect of  $M$  gets weaker and  $E$  declines slower than  $M^{-4}$ . There is still a little deviation from  $M^{-2.5}$  theory of Tabeling and Chabrerie (1981). However, if the maximum norm equation 65 is taken, we can confirm the  $M^{-2.5}$  theory as shown by red points. To be precise, each section of the data is labelled with  $\alpha_M$  produced by linear fitting. Overall, maximum norm indicates slower suppression laws with smaller  $|\alpha_M|$  for each section than those of the energy norm. The reason is presented in the following subsection 5.3.



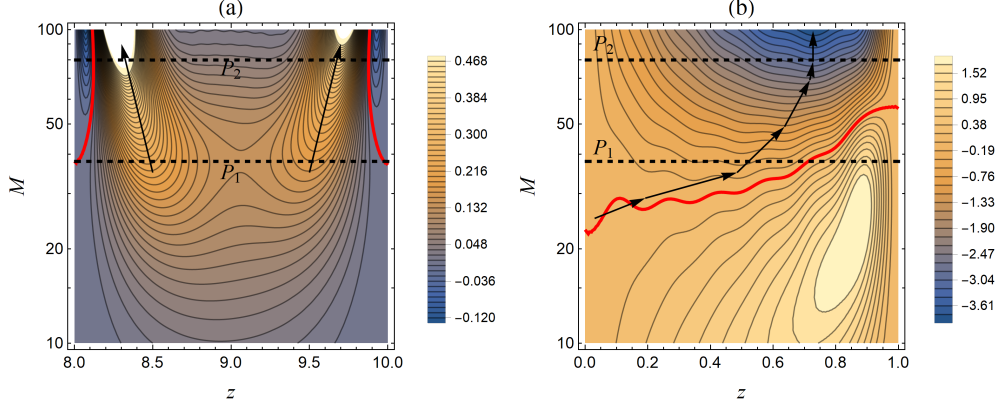


Figure 11: (a) radial profile of stream function  $w$  of secondary flow with varying  $M$  at  $z = 0$ . (b) axial profile of azimuthal vorticity  $\text{rot}_\theta \mathbf{v}$  with varying  $M$  on the inner torus wall (at  $r = r_1$ ). Red curves are zero-contour.

### 5.3 relationship between scale formula and secondary flow

The shift of the scale formula can be understood through the varied patterns of secondary flow. The analysis of Baylis and Hunt (1971) takes account into  $u_r$  but neglects  $u_z$ , and finally deduces  $E \sim M^{-4}$ . Before the critical point  $P_1$ , the secondary flow is trapezoid pattern, in which  $u_r$  near Hartmann layers is predominant, as shown in figure 9 (e). In this context  $M^{-4}$  theory is accurate in trapezoid pattern. To detect the exact shift point  $P_1$  when vortices begin cracking, we define radial profile of secondary flow:

$$w_r = M^4 \int_0^1 w_1 dz. \quad (69)$$

The continuous variations of  $w_r$  with Hartmann number are shown in figure 11 (a). We can see that when  $M \approx 30 \sim 40$ , the single peak of  $w$  crack into two peaks. This is also when  $M^{-4}$  theory becomes invalid. As  $M$  rises, the two peaks move away from each other. Meanwhile,  $w$  become lower in the middle region, leading to the low  $v_2$  in middle region shown in figure 9(f). This low value region expands as  $M$  increases. Hence, the suppression of  $M$  on inertial perturbation become faster as shown in  $P_1$ - $P_2$  part of figure 10. However, when  $M$  becomes larger than 80 (after  $P_2$ ), the expansion of low-value region stops while the reverse vortices get larger. This is the separation pattern as stated before. The reverse vortices bring in great  $u_z$  near Shercliff layer. The analysis of Tabeling and Chabrierie (1981) takes account into  $u_z$  then deduces  $E \sim M^{-2.5}$ . In this context,  $M^{-2.5}$  theory is accurate in separation pattern. Moreover, since  $M^{-2.5}$  theory only concerns the perturbation near Shercliff layer, the maximum norm (red points in figure 10) gives closer results than spatial-average energy norm.

To depict how the reverse vortices develop, the azimuthal vorticity,

$$\text{rot}_\theta \mathbf{v} = \frac{\partial v_r}{\partial z} - \frac{\partial v_z}{\partial r}, \quad (70)$$

are calculated with different  $M$  on the inner torus wall. Figure 11 (b) shows the results of  $M^2 \text{rot}_\theta \mathbf{v}$ . The coefficient  $M^2$  aims at clearer contours to offset the decrease in magnitude of vorticity. The red curves are zero-value contours, below which no reverse vortex exists. It is noticed that the reverse vortices partly occur near  $z = 0$  when  $M \approx 20$ . Then as  $M$  increases, the reverse region expands to the whole range of  $z = 0 \sim 1$ .  $M = 38$  is an important point when the sign of average vorticity shifts. This critical point is also very close to  $P_1$  where trapezoid pattern shifts into cracking pattern. The peak of reverse vorticity moves outwards as arrows show. When  $M > 80$ , the place of peak value is static, which marks the entry into separation pattern and  $\sim M^{-2.5}$  theory.

## 6 Conclusions

In terms of method, we have proposed a cost-effective semi-analytical algorithm for the MHD flow in annular channel. Two sub-schemes are involved: the Spectral-Galerkin scheme for primary flow and the perturbation method allowing for the secondary flow and inertial effect. The former has an unconditional convergence, while the convergence domain of the latter is proved to be  $Re' = Re/M < \kappa^{-2.5}$ . The semi-analytical solution is validated by the comparison with experiment and simulation. The fast computation makes it practicable to perform a large number of simulations with continuously changing operation conditions, which contribute to the exploration of flow pattern and scale laws.

In inertialess regime, a posteriori analysis of flow patterns has been conducted. First, the map of average velocity based on 40,000 cases in  $\eta$ - $M$  space is the main result. The phenomenological classification of flow patterns become clear at a glance in the map. Second, the electrically coupling demarcation of  $\eta$ - $M$  space is drawn. This curve indicates flow field and electric field can be decoupled when  $M \ll 1$  or  $M/\eta^2 \ll 1$ , while the curvature  $\kappa$  has marginal effect on the electrically coupled modes. Third, seven distinct flow patterns are identified. When  $\eta \ll 1$  and  $M$  is not large, only Shercliff layers exist and this pattern is examined for the first time. The proposed semi-analytic spectral solution recovers all patterns throughout the whole  $\eta$ - $M$  space.

In inertial regime, we examine the relationship between suppression law on inertial effect and the condition of vortexes in secondary flow. 120 cases with different Hartmann numbers ranging form 1 to 400 are calculated to explore the suppression law. It is identified that as  $M$  increase, the vortexes of secondary flow undergo four different conditions: (1) a pair of oval toroidal vortexes, (2) a pair of trapezoid vortexes, (3) two pairs of vortexes, (4) two pairs of main large vortexes with two pairs of thin anomalous reverse vortexes. In the first two stage of oval and trapezoid vortexes, the proposed semi-analytic spectral solution coincides with the  $Re^2/M^4$  suppression theory of Baylis and Hunt (1971). However, as  $M$  rise up to 40, the pair of trapezoid vortexes begin to crack into two pairs. Semi-analytic solutions see faster drop in inertial effect as  $Re^2/M^5$ . After that, when  $M > 80$ , the anomalous reverse vortexes are fully developed near Shercliff layers resulting in the slower suppression mode of  $Re^2/M^{2.5}$ , which coincides with the theory of Tabeing and Chabrerie (1981).

## Appendix A: basis function

Because of the radial boundary coordinates  $r = (1 \pm \kappa)/\kappa\eta$ , it is convenient to set  $x = \eta r$  and  $g_n(x) = u_{r,n}(r)$  and  $s_n(x) = h_{r,n}(r)$ . Substituting this transformation into equation14, we can get two Sturm-Liouville system for the radial function  $g$  as:

$$\frac{d}{dx} \left( \frac{1}{x} \frac{dg_n}{dx} \right) = -\alpha_n^2 \frac{1}{x} g_n, \quad g_n|_{x=\frac{1\pm\kappa}{\kappa}} = 0 \quad (71)$$

with the eigenvalues  $\alpha_n$  and the weight function  $1/x$ . It leads to the orthogonal function space  $g_n, n = 1, 2, 3\dots$  and the normalized solution:

$$g_n(x; \kappa, \alpha_n) = \frac{xJ_1(\alpha_n x)}{J_1(\alpha_n \frac{1+\kappa}{\kappa})} - \frac{xY_1(\alpha_n x)}{Y_1(\alpha_n \frac{1+\kappa}{\kappa})}, \quad (72)$$

where  $J_1$  is the 1-order Bessel function and  $Y_1$  is the 1-order Neumann function. The eigenvalues  $\alpha_n$  are determined by the boundary condition:

$$g_n\left(\frac{1-\kappa}{\kappa}; \kappa, \alpha_n\right) = 0. \quad (73)$$

When  $n \gg 1$ , there is the approximate formula:

$$\alpha_n \approx \frac{n\pi}{2} \quad (74)$$

Similarly, for  $s_n(x)$  we have:

$$\frac{d}{dx} \left( \frac{1}{x} \frac{ds_n}{dx} \right) = -\beta_n^2 \frac{1}{x} s_n, \quad \frac{ds_n}{dx} \Big|_{x=\frac{1\pm\kappa}{\kappa}} = 0 \quad (75)$$

with the eigenvalues  $\beta_n$  and the weight function  $1/x$ . It leads to the orthogonal function space  $s_n, n = 1, 2, 3\dots$ :

$$s_n(x; \kappa, \beta_n) = \frac{xJ_1(\beta_n x)}{J_0(\beta_n \frac{1+\kappa}{\kappa})} - \frac{xY_1(\beta_n x)}{Y_0(\beta_n \frac{1+\kappa}{\kappa})}, \quad (76)$$

The eigenvalues  $\beta_n$  are determined by the boundary condition:

$$\partial_x s_n\left(\frac{1-\kappa}{\kappa}; \kappa, \beta_n\right) = 0. \quad (77)$$

Note that  $\beta_1 = 0$  and  $s_1(x; \kappa, 0) \rightarrow 1$ . When  $n \gg 1$ , there is the approximate formula:

$$\beta_n \approx \frac{(n-1)\pi}{2} \quad (78)$$

Then we define the integral operator:

$$\langle f_1, f_2 \rangle \equiv \int_{r_1}^{r_2} f_1 f_2 / r dr \equiv \int_{\frac{1-\kappa}{\kappa}}^{\frac{1+\kappa}{\kappa}} f_1 f_2 / x dx \quad (79)$$

The orthogonal law of Sturm-Liouville theory states:

$$\text{if } i \neq j, \quad \langle g_i, g_j \rangle = \langle s_i, s_j \rangle = 0. \quad (80)$$

After resetting the normalized  $u_{r,n} = g_n(x)/\sqrt{\langle g_n, g_n \rangle}$  and  $h_{r,n} = s_n(x)/\sqrt{\langle s_n, s_n \rangle}$  we obtain the equation 17

## Appendix B: weak solution

Taking equation21 into the derivative of equation20 we obtain:

$$\langle u_{r,i}, h_{r,j} \rangle h_{z,j}'''' - \left( (M^2 + \eta^2 \alpha_i^2) \langle u_{r,i}, h_{r,j} \rangle + \langle u_{r,i}, h_{r,j} \rangle \eta^2 \beta_j^2 \right) h_{z,j}'' + \eta^2 \alpha_i^2 \langle u_{r,i}, h_{r,j} \rangle \eta^2 \beta_j^2 h_{z,j} = \langle S_w, u_{r,i} \rangle \quad (81)$$

If we define the matrix as:

$$\mathbf{u}_z = \begin{bmatrix} u_{z,1} \\ \vdots \\ u_{z,m} \end{bmatrix}, \mathbf{h}_z = \begin{bmatrix} h_{z,1} \\ \vdots \\ h_{z,m} \end{bmatrix}, \boldsymbol{\alpha} = \begin{bmatrix} \alpha_1^2 & & \\ & \ddots & \\ & & \alpha_m^2 \end{bmatrix}, \boldsymbol{\beta} = \begin{bmatrix} \beta_1^2 & & \\ & \ddots & \\ & & \beta_m^2 \end{bmatrix} \quad (82)$$

and

$$\boldsymbol{\tau} = [\tau_{i,j} \rightarrow \langle u_{r,i}, h_{r,j} \rangle], \quad \boldsymbol{\gamma} = [\gamma_{i,j} \rightarrow \langle u_{r,i}, h_{r,j} \rangle^{-1} \langle S_w, u_{r,i} \rangle], \quad 1 \leq i, j \leq m \quad (83)$$

$$\mathbf{B} = \begin{bmatrix} 0 & \mathbf{E} \\ -\eta^4 (\boldsymbol{\tau}^{-1} \boldsymbol{\alpha} \boldsymbol{\tau}) \boldsymbol{\beta} & \eta^2 \boldsymbol{\beta} + \eta^2 \boldsymbol{\tau}^{-1} \boldsymbol{\alpha} \boldsymbol{\tau} + M^2 \mathbf{E} \end{bmatrix} \quad (84)$$

where  $\mathbf{E}$  is the  $m$ -order identity matrix and  $\mathbf{B}$  is the  $2m$ -order square matrix. Then equation 81 becomes

$$\frac{d^2}{dz^2} \begin{bmatrix} \mathbf{h}_z \\ \mathbf{h}_z'' \end{bmatrix} = \mathbf{B} \begin{bmatrix} \mathbf{h}_z \\ \mathbf{h}_z'' \end{bmatrix} + \begin{bmatrix} \mathbf{0} \\ \boldsymbol{\gamma} \end{bmatrix} \quad (85)$$

To solve this differential equations set, we must calculate the eigenvalues  $\chi$  and eigenvectors  $\mathbf{Q}$  of  $\mathbf{B}$ :

$$\mathbf{Q}^{-1} \mathbf{B} \mathbf{Q} = \text{Diag} [\chi_i]_{1 \leq i \leq 2m} \quad (86)$$

The solution is:

$$\begin{bmatrix} \mathbf{h}_z \\ \mathbf{h}_z'' \end{bmatrix} = \mathbf{Q} \text{Diag} \begin{bmatrix} \frac{\sinh(\sqrt{\chi_i} z)}{\sinh(\sqrt{\chi_i})} \\ \frac{\cosh(\sqrt{\chi_i} z)}{\sinh(\sqrt{\chi_i})} \end{bmatrix} \mathbf{C} \quad (87)$$

Given  $h$ , the solution to  $u$  is:

$$\mathbf{u}_z = \frac{1}{\eta^2 M} \boldsymbol{\alpha}^{-1} \boldsymbol{\tau} [M^2 \mathbf{E} + \eta^2 \boldsymbol{\beta}; \quad -\mathbf{E}] \mathbf{Q} \text{Diag} \begin{bmatrix} \sqrt{\chi_i} \frac{\cosh(\sqrt{\chi_i} z)}{\sinh(\sqrt{\chi_i})} \\ \frac{\sinh(\sqrt{\chi_i} z)}{\sinh(\sqrt{\chi_i})} \end{bmatrix} \mathbf{C} \quad (88)$$

where  $\mathbf{C}$  is a constant array that shall be determined by the boundary condition9.

## Appendix C: convergence of spectral-Galerkin series

To examine the convergence of this spectral-Galerkin series, we observe the magnitude of each  $n^{\text{th}}$  term in series 16 and define  $C_n$  as

$$C_n = \frac{\|u_{r,n}(r)u_{z,n}(z)\|}{\|u_{r,1}(r)u_{z,1}(z)\|} \quad (89)$$

The spectral-Galerkin operation involves  $M$ ,  $\eta$  and  $\kappa$  in  $C_n$ . Figure 12 (a) compares the decline of  $C_n$  with various  $M$ , while (b) and (c) illustrate the effect of geometric parameters  $\eta$  and  $\kappa$ . It is noticed that although the smaller  $M$ ,  $\eta$  and  $\kappa$  can lead to smaller  $C_n$  ( $n > 1$ ), the rate of decay in all the cases levels off to  $1/n^3$ . In that context, three important conclusions are reached:

1. The nature of convergence of the method is free of Hartmann number  $M$ , geometric parameters  $\eta$  and  $\kappa$ . In other words, the convergence is **unconditional**.
2. The speed of convergence is  $\sim 1/n^3$ .
3. Considering the last item, if series 16 is truncated by the  $N^{\text{th}}$  term, the round-off error will be at the level of  $\sim 1/N^2$ .

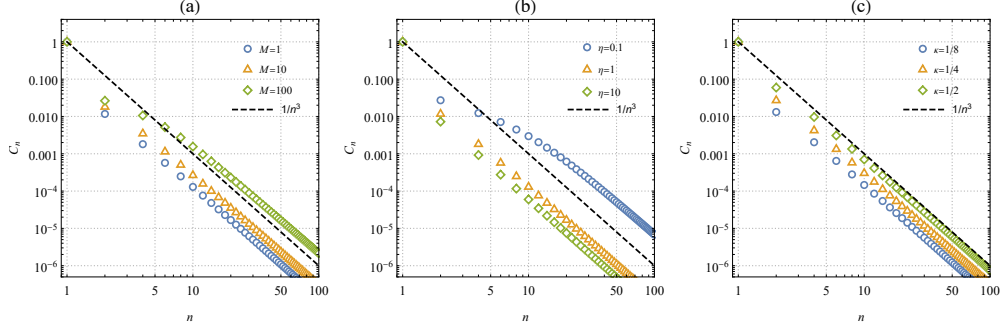


Figure 12: Magnitude of each term in series 16 (a) with varying  $M$  at  $\eta = 1$  and  $\kappa = 1/9$ ; (b) with varying  $\eta$  at  $M = 1$  and  $\kappa = 1/9$ ; (c) with varying  $\kappa$  at  $M = 1$  and  $\eta = 1$ . The dashed line is  $1/n^3$

## Appendix D: convergence of perturbation expansion

The applicability of  $Re$  rest with the domain of convergence of perturbation expansion<sup>10</sup>. Mathematically accuracy convergence domain is beyond the scope of our investigation. Nevertheless, an estimation of convergence can be fruitful. In this estimation, we take  $\eta \sim 1$ ,  $M \gg 1$  and  $\kappa < 1$ , which are the common case in the previous study (Baylis and Hunt, 1971; Moresco and Alboussière, 2004; Zhao and Zikanov, 2012; Poyé et al., 2020) Scale analysis of equation<sup>13</sup> shows:

$$w_1 \sim \kappa^2 u_0^2 / M^2 \quad (90)$$

Similarly equation<sup>13</sup> implicates (note that the boundary layer make  $M\partial_z h \sim 1$ ):

$$u_2 \sim \kappa u_0 w_1 \sim \kappa^3 u_0^3 / M^2 \quad (91)$$

Then, for higher order,  $w_2 = 0$ , and

$$w_3 \sim \kappa^2 u_0 u_2 / M^2 \sim \kappa^5 u_0^4 / M^4 \quad (92)$$

At this point, it is clear that:

$$w = Re \sum_{i=1} w_{2i-1} Re^{2i}, \quad w_{2i-1} \sim \kappa^{3i-1} u_0^{2i} / M^{2i} \quad (93)$$

Mathematically, the convergence domain shall be approximately:

$$\frac{Re^2 u_0^2}{M^2} < \frac{1}{\kappa^3} \quad (94)$$

Moreover, equation<sup>39</sup> implicates that when  $M \ll 1$

$$u_0 \sim \bar{v} \sim \frac{1}{2} \ln \left( \frac{1+\kappa}{1-\kappa} \right) \sim \kappa + O(\kappa^3). \quad (95)$$

Thus, the convergence domain is

$$Re' = \frac{Re}{M} < \frac{1}{\kappa^{2.5}} \quad (96)$$

## Acknowledgement

This work is supported by the National Natural Science Foundation of China (Grant No. 43211872093). We also wish to thank Dr. Alexandre Poyé from CNRS and Prof. Thomas M. York from the Ohio State University for the fruitful discussion.

## Declaration of Interests

The authors report no conflict of interest.

## References

- Balbus, S. A. and Hawley, J. F. (1998). Instability, turbulence, and enhanced transport in accretion disks. *Rev. Mod. Phys.*, 70(1):53. Number: 1.
- Baylis, J. A. (1964). Detection of the Onset of Instability in a Cylindrical Magnetohydrodynamic Flow. *Nature*, 204(4958):563–563. Number: 4958.
- Baylis, J. A. (1971). Experiments on laminar flow in curved channels of square section. *Journal of Fluid Mechanics*, 48(3):417–422. Number: 3.
- Baylis, J. A. and Hunt, J. C. R. (1971). MHD flow in an annular channel; theory and experiment. *Journal of Fluid Mechanics*, 48(3):423–428. Number: 3.
- Birkhoff, G. and Merzbach, U. C. (1973). *A source book in classical analysis*, volume 20. Harvard University Press Cambridge, MA.
- Boisson, J., Monchaux, R., and Aumaître, S. (2017). Inertial regimes in a curved electromagnetically forced flow. *Journal of Fluid Mechanics*, 813:860–881.
- Davidson, P. A. (2016). *Introduction to Magnetohydrodynamics*. Cambridge University Press, 2 edition.
- Duncan, W. (1848). The principles of the galerkin method. *R. & M*, 1938.
- Gottlieb, D. and Orszag, S. A. (1977). *Numerical analysis of spectral methods: theory and applications*. SIAM.
- Khalzov, I. V., Ilgisonis, V. I., Smolyakov, A. I., and Velikhov, E. P. (2006). Magnetorotational instability in electrically driven flow of liquid metal: Spectral analysis of global modes. *Physics of Fluids*, 18(12):124107. Number: 12.
- Khalzov, I. V., Smolyakov, A. I., and Ilgisonis, V. I. (2010). Equilibrium magnetohydrodynamic flows of liquid metals in magnetorotational instability experiments. *Journal of Fluid Mechanics*, 644:257–280.
- Larmor, J. (1919). Possible rotational origin of magnetic fields of sun and earth. *Elec. Rev.*, 85:412.
- Moresco, P. and Alboussière, T. (2004). Experimental study of the instability of the Hartmann layer. *Journal of Fluid Mechanics*, 504:167–181.
- Pothérat, A., Sommeria, J., and Moreau, R. (2000). An effective two-dimensional model for MHD flows with transverse magnetic field. *Journal of Fluid Mechanics*, 424:75–100.
- Poyé, A., Agullo, O., Plihon, N., Bos, W. J. T., Desangles, V., and Bousselin, G. (2020). Scaling laws in axisymmetric magnetohydrodynamic duct flows. *Physical Review Fluids*, 5(4):043701. Number: 4.
- Shercliff, J. A. and Batchelor, G. K. (1953). Steady motion of conducting fluids in pipes under transverse magnetic fields. *Mathematical Proceedings of the Cambridge Philosophical Society*, 49(01):136.
- Stelzer, Z., Miralles, S., Cébron, D., Noir, J., Vantieghem, S., and Jackson, A. (2015). Experimental and numerical study of electrically driven magnetohydrodynamic flow in a modified cylindrical annulus. II. Instabilities. *Physics of Fluids*, 27(8):084108. Number: 8.
- Tabeling, P. (1982). Sequence of Instabilities in Electromagnetically Driven Flows between Conducting Cylinders. *Physical Review Letters*, 49(7):460–463. Number: 7.
- Tabeling, P. and Chabrierie, J. P. (1981). Magnetohydrodynamic secondary flows at high Hartmann numbers. *Journal of Fluid Mechanics*, 103(-1):225. Number: -1.
- Vantieghem, S. and Knaepen, B. (2011). Numerical simulation of magnetohydrodynamic flow in a toroidal duct of square cross-section. *International Journal of Heat and Fluid Flow*, 32(6):1120–1128. Number: 6.
- Zhang, K., Wang, Y., Tang, H., Li, Y., Wang, B., York, T. M., and Yang, L. (2020). Two-dimensional analytical investigation into energy conversion and efficiency maximization of magnetohydrodynamic swirling flow actuators. *Energy*, 209:118479.
- Zhao, Y. and Zikanov, O. (2012). Instabilities and turbulence in magnetohydrodynamic flow in a toroidal duct prior to transition in Hartmann layers. *Journal of Fluid Mechanics*, 692:288–316.